Journal of Catalysis 271 (2010) 239–250

Contents lists available at ScienceDirect

Journal of Catalysis

journal homepage: www.elsevier.com/locate/jcat

Correlating extent of Pt–Ni bond formation with low-temperature hydrogenation of benzene and 1,3-butadiene over supported Pt/Ni bimetallic catalysts

William W. Lonergan, Dionisios G. Vlachos, Jingguang G. Chen *

Department of Chemical Engineering, Center for Catalytic Science and Technology (CCST), University of Delaware, Newark, DE 19716, USA

ARTICLE INFO

Article history:
Received 1 December 2009
Revised 20 January 2010
Accepted 21 January 2010
Available online 25 February 2010

Keywords:
Pt/Ni bimetallic catalysts
Hydrogenation
Benzene
1,3-Butadiene
EXAFS

ABSTRACT

Low-temperature hydrogenation of benzene and 1,3-butadiene on supported Pt/Ni catalysts have been used as probe reactions to correlate hydrogenation activity with the extent of Pt–Ni bimetallic bond formation. Pt/Ni bimetallic and Pt and Ni monometallic catalysts were supported on γ-Al_2O_3 using incipient wetness impregnation. Two sets of bimetallic catalysts were synthesized: one set to study the effect of metal atomic ratio and the other to study the effect of impregnation sequence. Fourier transform infrared spectroscopy (FTIR) CO adsorption studies were performed to characterize the surface composition of the bimetallic nanoparticles, and transmission electron microscopy (TEM) was utilized to characterize the particle size distribution. Batch reactor studies with FTIR demonstrated that all bimetallic catalysts outperformed monometallic catalysts for both benzene and 1,3-butadiene hydrogenation. Within the two sets of bimetallic catalysts, it was found that catalysts with a smaller Pt:Ni ratio possessed higher hydrogenation activity and that catalysts synthesized using co-impregnation had greater activity than sequentially impregnated catalysts. Extended X-ray absorption fine structure (EXAFS) measurements were performed in order to verify the extent of Pt–Ni bimetallic bond formation, which was found to correlate with the hydrogenation activity.

1. Introduction

Bimetallic catalysts often exhibit activities and selectivities that differ from those of the corresponding monometallic catalysts [1–3]. Due to these unique properties, bimetallic catalysts have been utilized in many different catalytic applications [4–6]. Early work on bimetallic catalysts also showed that the catalytic properties can be tuned by adjusting the relative amounts of the two metals [1]. By combining both experimental studies and theoretical calculations, many fundamental investigations have been performed in an effort to correlate the electronic properties of bimetallic surfaces to chemical reactivities [2,3,7–14].

Recently, the structure of bimetallic surfaces has been found to influence electronic and catalytic properties [7,9,12,13,15–17]. Research in our group has focused on the Ni/Pt(1 1 1) monolayer bimetallic system in which a monolayer of Ni atoms are located either on the surface, resulting in a Ni-terminated Ni–Pt–Pt(1 1 1) surface or in the subsurface region, giving a Pt-terminated Pt–Ni–Pt(1 1 1) subsurface structure [15]. These two surfaces exhibit distinct properties that differ either from monometallic surface or from each other [13,15,16,18]. Specifically, atomic hydrogen and alkenes bind more weakly to the Pt–Ni–Pt(1 1 1) surface than to Ni–Pt–Pt(1 1 1) and the monometallic surfaces, leading to a novel low-temperature hydrogenation pathway on the Pt–Ni–Pt(1 1 1) subsurface structure [13]. A similar hydrogenation pathway is also observed on a Pt/Ni(1 1 1) surface prepared by depositing a monolayer (ML) of Pt on Ni(1 1 1) [19]. Conversely, the Ni–Pt–Pt(1 1 1) surface binds adsorbates more strongly than Pt–Ni–Pt(1 1 1) and the monometallic surfaces [16], making the Ni–Pt–Pt(1 1 1) surface more active for reforming of oxygenates, such as ethylene glycol and glycerol to produce H_2 [16,20]. The different binding energies on the subsurface Pt–Ni–Pt(1 1 1) and surface Ni–Pt–Pt(1 1 1) structures have been explained based on the location of the surface d-band center from density functional theory (DFT) calculations [21].

Combined experimental and theoretical studies on the thermodynamic stability of the Ni/Pt(1 1 1) monolayer bimetallic surfaces reveal that the Ni monolayer can migrate in the presence of adsorbates. For instance, the Pt–Ni–Pt(1 1 1) subsurface structure is found to be stable either in vacuum or with adsorbed atomic hydrogen [22]; however, in the presence of adsorbed oxygen, Ni atoms will segregate to the surface to create the Ni–Pt–Pt(1 1 1) surface [23,24]. The activation barrier for the transformation between subsurface and surface structures is relatively low, ~15 kcal/mol, signifying that Ni atoms may diffuse and segregate during calcination and reduction procedures and under reaction conditions. Similar behavior has been observed for monolayer Ni

* Corresponding author. Fax: +1 302 831 2085.
E-mail address: jgchen@udel.edu (J.G. Chen).

0021-9517/$ - see front matter © 2010 Elsevier Inc. All rights reserved.
doi:10.1016/j.jcat.2010.01.019

on a polycrystalline Pt substrate under in situ conditions, where Ni atoms diffuse into the subsurface region in the presence of H_2 and segregate to the surface in the presence of O_2 [25]. A recent X-ray photoelectron spectroscopy (XPS) study found similar results for supported Pt/Ni catalysts in which in the reducing environment of H_2 Pt migrates to the surface, while in an O_2 environment, Ni segregates to the surface to form a NiO skin [26].

In a previous study on Pt/Ni catalysts, it was reported that the activities for the disproportionation (self-hydrogenation) of cyclohexene and the selective hydrogenation of acetylene in the presence of ethylene could be affected by whether Ni or Pt was impregnated first [27]. The primary objective of the work presented in this paper is to correlate the effects of Pt:Ni atomic ratio and impregnation sequence with the extent of Pt–Ni bimetallic bond formation and with the low-temperature hydrogenation activity of benzene and 1,3-butadiene. The effect of metal atomic ratio was studied by synthesizing bimetallic catalysts with Pt:Ni ratios of 1:1, 1:3, and 1:10. Impregnation sequence was investigated by synthesizing catalysts using either a Ni-first or a Pt-first sequential impregnation or a simultaneous co-impregnation. Extended X-ray absorption fine structure (EXAFS) and transmission electron microscopy (TEM) were used to characterize the extent of bimetallic formation and particle size, respectively. In order to study the effects of these two series of catalysts on the hydrogenation of conjugated systems, benzene and 1,3-butadiene hydrogenation were chosen as probe reactions because they serve both fundamental and practical purposes.

Benzene hydrogenation to cyclohexane is an important industrial reaction because it can be utilized to reduce the aromatic content of petroleum fuels [28,29], and in the production of commodity chemicals, the cyclohexane products can be further reacted to produce adipic acid and caprolactum which are two of the intermediates in the production of nylon [30]. A number of different transition metal-based catalysts such as Ni [31–39], Pt [40,41], Pd [42,43], Ru [44–47], Fe [48–50], and Co [51–55] have been studied for use in benzene hydrogenation. Commonly, Pt- and Ni-based catalysts are used in commercial processes to produce cyclohexane, while Ru-based catalysts are commonly used to partially hydrogenate benzene to cyclohexene [47].

The hydrogenation of 1,3-butadiene serves as a means to purify the butene stream generated in the cracking of naphtha or gas oil. In order to successfully polymerize butene, 1,3-butadiene must be removed, because even small amounts of 1,3-butadiene (up to 1%) are sufficient to poison the polymerization catalysts [56]. Catalysts based on Pd [57–60] and Pt [60,61] are commonly studied for use in 1,3-butadiene hydrogenation. Pd supported on alumina has been reported as the most active and selective catalyst for the selective hydrogenation of dienes; however, some literature shows that Pt/Ni bimetallic catalysts exhibit both high activity and selectivity to 1,3-butadiene hydrogenation [60].

2. Experimental

2.1. Catalyst preparation

The γ-Al_2O_3-supported catalysts were synthesized using incipient wetness impregnation. Two sets of bimetallic catalysts were synthesized: one set to study the effect of impregnation sequence and the other to study the effect of Pt:Ni atomic ratio. Three control monometallic catalysts were also synthesized: 1.7 wt.% Pt/γ-Al_2O_3, 1.5 wt.% Ni/γ-Al_2O_3, and 5.0 wt.% Ni/γ-Al_2O_3. To study the effect of impregnation sequence, three catalysts with Pt:Ni atomic ratio of 1:3 were synthesized with the following sequences: Ni-first, Pt-first, and co-impregnation. A series to study the effect of Pt:Ni atomic ratio was synthesized using the Ni-first impregnation for the following Pt:Ni ratios: 1:1, 1:3, and 1:10. Table 1 lists the synthesized catalysts, their metal loadings, and the nomenclature that will be used to identify them for the remainder of this paper.

Pt and Ni precursor solutions were made by adding the necessary volume of deionized water to the $Pt(NH_3)_4(NO_3)_2$ (Alfa Aesar) and $Ni(NO_3)_2{\cdot}6H_2O$ (Alfa Aesar) precursor salts. Catalysts were dried at 373 K for 10 h and calcined at 563 K for 2 h. Sequentially impregnated catalysts were dried and calcined at the same conditions after each impregnation.

2.2. Catalyst characterization

2.2.1. Pulse CO chemisorption

Pulse chemisorption using an AMI-200ip (Altamira Instruments) was performed to determine the carbon monoxide (CO) uptake and metal dispersion. Approximately 0.1 g of catalyst was loaded into a quartz reactor and reduced under a hydrogen–helium mixture (50% H_2/He) at 723 K for 1 h. After cooling in He, pulse CO chemisorption was performed at room temperature using pulses of 20 cm^3 min^{-1} CO in a He carrier gas. A thermal conductivity detector (TCD) was used to monitor the flow of CO out of the quartz reactor. Metal dispersion was calculated from the CO chemisorption measurements assuming a stoichiometry of M:CO = 1:1 (M = Pt, Ni). Both the metal dispersion and CO uptake results are shown in Table 2. Due to the uncertainty in stoichiometry and surface compositions of the bimetallic catalysts, the dispersion values in Table 2 might not be very meaningful, but are listed to provide a relative ranking of metal dispersion. However, the amount of adsorbed CO provides a quantitative comparison of the number of active sites among the two series of catalysts. The data in Table 2 show that both Pt and Ni monometallic catalysts adsorb CO at room temperature. Inspection of the two series of bimetallic catalysts shows that as the amount of Ni in the catalysts increases, the CO uptake increases and that impregnation sequence does not affect the amount of CO adsorbed by the catalysts.

2.2.2. FTIR studies

Fourier transform infrared (FTIR) spectroscopy was used to measure the adsorption sites of CO on the different catalysts as well as to monitor the gas-phase concentrations of reactants and products during the hydrogenation of benzene and 1,3-butadiene. The design of the IR cell was based on a design reported elsewhere in the literature [62]. Fitted with BaF_2 windows, the stainless steel IR cell allowed for in situ reduction of samples and spectroscopic measurements of either surface adsorbates or gas-phase species. Spectra were recorded with 4-cm^{-1} resolution using a Thermo Nicolet Nexus 470 spectrometer equipped with a MCT-A (mercury cadmium telluride) detector.

Catalysts were supported in the reactor by pressing the catalyst powder onto a tungsten mesh (1×2.4 cm, 100 mesh, 0.025 cm wire diameter, Alfa Aesar) at a force of 3 tons. The tungsten mesh was then attached to a nickel mounting bracket connected at the end of a z-translating manipulator and feedthrough. A K-type thermocouple was attached to the mesh to monitor the temperature of the catalyst during reduction and reaction. The feedthrough provided connections for the thermocouple and leads for resistive heating of the catalyst through the tungsten mesh. The gases and liquid vapors used for reduction, adsorption studies, and hydrogenation reactions were introduced into the IR cell through a gas manifold maintained under high vacuum conditions.

For all FTIR experiments, ~25 mg of supported catalyst was loaded into the IR cell as described above. Before each experiment, the IR cell and gas manifold were evacuated to a pressure below 10^{-6} Torr for 1 h in order to remove water and other impurities. The catalyst was then reduced at 723 K in 30 Torr of hydrogen

Table 1
Catalyst compositions and nomenclature.

Catalyst	Metal content (wt.%)		Atomic ratio (Pt:Ni)	Impregnation sequence	Nomenclature
	Pt	Ni			
1.7%Pt/γ-Al_2O_3	1.7	–	–	–	1Pt/γ-Al_2O_3
1.5%Ni/γ-Al_2O_3	–	1.5	–	–	3Ni/γ-Al_2O_3
5.0%Ni/γ-Al_2O_3	–	5.0	–	–	10Ni/γ-Al_2O_3
1.7%Pt–0.5%Ni/γ-Al_2O_3	1.7	0.5	1:1	Ni-first	1Pt–1Ni/γ-Al_2O_3
1.7%Pt–1.5%Ni/γ-Al_2O_3	1.7	1.5	1:3	Ni-first	1Pt–3Ni/γ-Al_2O_3
1.7%Pt–5.0%Ni/γ-Al_2O_3	1.7	5.0	1:10	Ni-first	1Pt–10Ni/γ-Al_2O_3
1.5%Ni–1.7%Pt/γ-Al_2O_3	1.7	1.5	1:3	Pt-first	3Ni–1Pt/γ-Al_2O_3
1.5%Ni–1.7%Pt/γ-Al_2O_3	1.7	1.5	1:3	Co-impregnated	1Pt–3Ni(co-imp)/γ-Al_2O_3

Table 2
CO chemisorption results.

Catalyst	CO uptake (μmol CO/g catalyst)	Dispersion from chemisorption (%)
1Pt/γ-Al_2O_3	17.4	20.3
3Ni/γ-Al_2O_3	14.4	5.6
10Ni/γ-Al_2O_3	27.9	10.9
1Pt–1Ni/γ-Al_2O_3	12.8	14.3
1Pt–3Ni/γ-Al_2O_3	23.5	14.5
1Pt–10Ni/γ-Al_2O_3	37.5	10.9
3Ni–1Pt/γ-Al_2O_3	22.0	13.5
1Pt–3Ni(co-imp)/γ-Al_2O_3	24.6	15.1

for 0.5 h. Following reduction, the cell was evacuated and the catalyst was flashed to 723 K to remove any surface species generated during reduction. This reduction cycle was repeated three times before performing FTIR experiments.

For CO adsorption studies, the catalyst was lowered into the IR beam in order to collect the surface background spectra. Then ~1 Torr of CO was introduced into the IR cell and kept there for 5 min at room temperature before evacuating the cell. Surface spectra of adsorbed CO were then collected.

The hydrogenation reactions were performed using the IR cell as a batch reactor. The purity of the benzene vapor and the 1,3-butadiene gas was verified in situ prior to experimentation by comparing the IR spectra with standard references reported in literature [63]. During the reactions, the gas-phase reactants and products were monitored by recording IR spectra (32 scans) every 30 s. Prior to the initiation of a reaction, a baseline for the reaction was determined by collecting IR spectra of the reactor cell under vacuum for 10 min. During the collection of the reaction baseline, the reactant species were premixed at room temperature within the gas manifold. For benzene hydrogenation, hydrogen gas and benzene vapor were mixed at a partial pressure ratio of 6:1, while for 1,3-butadiene hydrogenation, the ratio of hydrogen to 1,3-butadiene was 2.2:1. To start the reaction, the reactant gas mixture was quickly dosed into the IR cell while holding the catalyst at the desired reaction temperature. The hydrogenation reactions proceeded at catalyst temperatures of 343 and 308 K and initial pressures of ~8.0 and ~13.0 Torr for benzene and 1,3-butadiene, respectively.

For benzene hydrogenation, the concentrations of the two main gas-phase species (benzene and cyclohexane) were estimated using the intensities of their characteristic vibrational modes at 1810 cm^{-1} (overtone of the C—C stretching mode at 993 cm^{-1}) and 1458 cm^{-1} (—CH_2 deformation), respectively. The ωCH_2 vibrational mode (1139 cm^{-1}) of cyclohexene was also monitored; however, it was not observed in any of the reactions.

The concentration of 1,3-butadiene was determined using the peak intensity of the vibrational mode at 1586 cm^{-1} (C=C—C=C deformation mode). 1-Butene was determined to be the only butene produced from the hydrogenation of 1,3-butadiene because no peaks corresponding to cis-2-butene were observed, which in turn suggested that no trans-2-butene was present either, because it would be expected that the two isomers would be under thermodynamic equilibrium. In the absence of cis-2-butene or trans-2-butene, the concentration of 1-butene was calculated using the intensity of the vibrational mode at 1655 cm^{-1} (C=C deformation). The concentration of butane was estimated by calculating the intensity of 1-butene at 1466 cm^{-1} (CH_3 deformation) and subtracting that from the total intensity at 1466 cm^{-1}, resulting in the intensity corresponding to butane. This calculation is summarized in Eq. (1):

$$Intensity_{Butane(1466)} = Intensity_{Total(1466)} - Conc_{1-Butene(1655)}\left(\frac{Intensity_{1-Butene(1466)}}{Conc_{1-Butene(1466)}}\right) \quad (1)$$

All carbon atoms were accounted for by performing a carbon balance, confirming the absence of cis-2-butenes and trans-2-butenes.

The different extinction coefficients for all the gas-phase reactants and products were accounted for by calibrating the intensity of the characteristic FTIR peak as a function of concentration of each molecule. The intensity of each peak was measured at a number of pressures in a range relevant to each reaction. Using the volume of the reactor cell and the ideal gas law, gas-phase concentrations were calculated based on the pressure-intensity calibration for each molecule.

2.2.3. Transmission electron microscopy (TEM)

TEM analysis was performed on spent catalysts using a JEOL 2010F equipped with a Schottky field emission gun operated at 200 keV, with an ultra-high resolution pole piece providing a point resolution of 1.9 Å. Energy dispersive X-ray spectroscopy (EDS) was used to perform elemental analysis on larger particles using an EDAX Phoenix X-ray spectrometer with a resolution of 134 eV over a 40 keV range. Imaging and EDS analysis were performed in scanning mode (STEM) using a 20 nm camera length and a 0.5 nm diameter nanoprobe. TEM samples were prepared by grinding and suspending spent catalysts in ethanol, and then a small amount of this solution was dropped onto a carbon-coated copper grid and allowed to dry before loading the sample into the TEM.

2.2.4. Extended X-ray absorption fine structure

EXAFS measurements of the Pt L_{III}-edge were collected in order to detect the formation of Pt–Ni bimetallic bonds. The EXAFS experiments were conducted on the X18B and X19A beamlines at the National Synchrotron Light Source (NSLS), Brookhaven National Laboratory. EXAFS samples were prepared by pressing the alumina-supported catalysts into self-supported pellets using a force of ~3 tons. The mass of the pellets was chosen so that the thickness of the samples was on the order of two absorption lengths in order to optimize the signal to noise ratio. The catalyst

pellets were loaded into an in-house designed EXAFS cell which allowed for in situ reduction and simultaneous collection of both transmission and fluorescence signals. The catalysts were reduced by heating under a diluted hydrogen flow (5% H_2 in He, 40 sccm) to 723 K with a heating rate of 10 K min^{-1}. The samples were held at 723 K for 1 h and then allowed to cool to room temperature under diluted H_2 flow. The Pt L_{III}-edge EXAFS were then collected at room temperature using a double crystal Si(1 1 1) monochromator. Ionization chambers were used to measure the incident and transmitted X-ray signals, while the fluorescence signal was collected using a 12-channel germanium detector. EXAFS measurements were also collected from a Pt foil in order to calibrate the edge energies of the measurements collected from the catalyst samples.

The EXAFS measurements were collected in three energy regions, each having a different step size and integration time: the pre-edge region from −150 eV to −25 eV before the edge, the near-edge region from −25 eV before the edge to 40 eV past the edge, and the post-edge region from 40 eV to 18*k* (approximately 1450 eV) past the edge. The step sizes and integration times used in the three regions were: 5 eV and 1 s for the pre-edge, 0.5 eV and 2 s for the near-edge, and 0.05*k* (approximately 3 eV) and 2 s for the post-edge.

The IFFEFIT 1.2.11 data analysis package (Athena, Artemis, Atoms, and FEFF6) was used to analyze and fit the EXAFS data [64,65]. The raw data were reduced by aligning the scans to the foil standard, deglitching when necessary, and merging multiple scans together to reduce experimental error. The AUTOBK algorithm in Athena was used to remove the isolated-atom background function from the EXAFS data and then the data were Fourier transformed into R-space. Local structural information was obtained by using Artemis to fit each data set with theoretical standards generated by FEFF6 [66] in R-space. Both the Pt–Pt and the Pt–Ni contributions to the theoretical EXAFS were taken into account in fitting the data for the bimetallic catalysts, while only Pt–Pt contributions were included in fitting the monometallic Pt catalyst. The theoretical Pt–Pt photoelectron amplitudes and phases were calculated for the bulk Pt fcc structure. Pt–Ni contributions were calculated theoretically in FEFF6 by using the same Pt fcc structure with the exception that the Pt atoms in the first nearest-neighbor shell were replaced with Ni atoms. The passive electron reduction factor (S_0^2) was found to be 0.85 from fitting of the Pt-foil data, and this value was fixed through the fitting of all the catalysts. The seven parameters used in the fitting procedure were the correction to the edge energy, the coordination numbers of the Pt–Pt and Pt–Ni bonds, corrections to their model interatomic distances, and their mean-square deviations in interatomic distances (EXAFS Debye–Waller factors).

3. Results

3.1. FTIR of adsorbed CO

The FTIR spectra of adsorbed CO on the two series of catalysts used to study the effects of metal atomic ratio and impregnation sequence are presented in Fig. 1a and b, respectively. Fig. 1a contains the CO adsorption data for the series of catalysts used to study the effect of metal atomic ratio. The intense high-frequency peak observed in each spectrum around 2060 cm^{-1} can be attributed to CO binding to the metals through the atop site [67–70]. The lower frequency peaks at 1846 cm^{-1} on 1Pt/γ-Al_2O_3 and 1945 cm^{-1} on 3Ni/γ-Al_2O_3 and 10Ni/γ-Al_2O_3 represent CO bound through bridge sites on the catalyst particles [67–70]. Ni is known to form $NiAl_2O_4$ with γ-Al_2O_3 [71]; however, the presence of both atop and bridge-bound CO in both Ni monometallic catalysts show that there is at least a fraction of Ni in the metallic state after reduction. Inspecting the spectra for the three bimetallic catalysts with increasing amounts of Ni, it is seen that at lower Ni loadings (Pt:Ni = 1:1, 1:3), the peaks associated with bridge-bound CO appear at frequencies similar to the CO bridge binding sites on 1Pt/γ-Al_2O_3, suggesting that CO is adsorbed on Pt atoms. However, on 1Pt–10Ni/γ-Al_2O_3, the bridge-bound CO frequency is similar to that on 10Ni/γ-Al_2O_3, suggesting that CO is most likely adsorbed on Ni atoms. This could be explained by the fact that there are ten times as many Ni atoms as Pt atoms, so Ni–CO vibrations would dominate the signal.

Fig. 1b displays the CO spectra for the series of catalysts used to study the effect of impregnation sequence. Once again considering only the bridge-bound CO as a means for comparison, the three

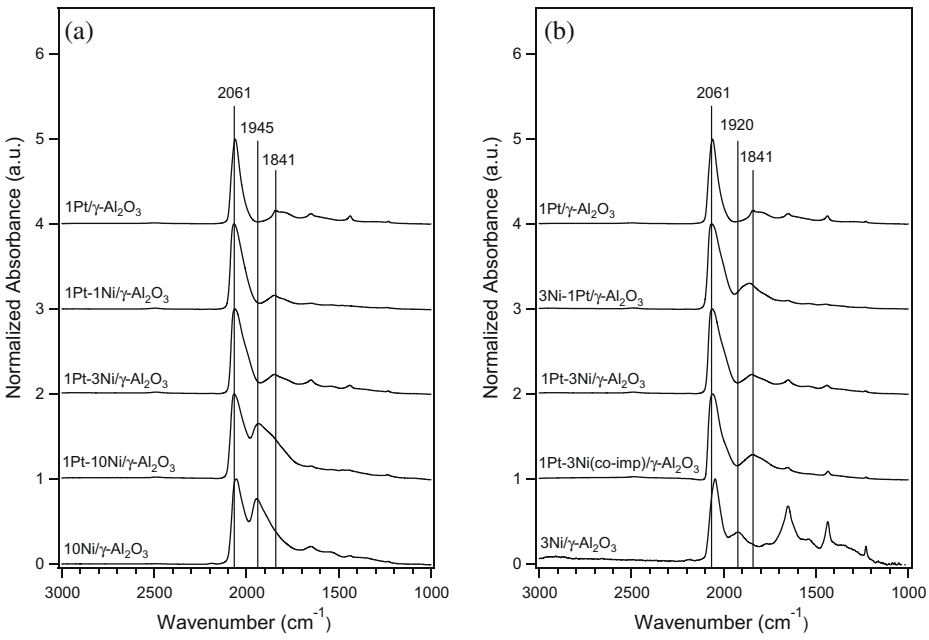

Fig. 1. Fourier transform infrared (FTIR) spectroscopy of CO adsorption (a) on the series of bimetallic catalysts with different metal atomic ratios, (b) on the series of bimetallic catalysts with different impregnation sequences.

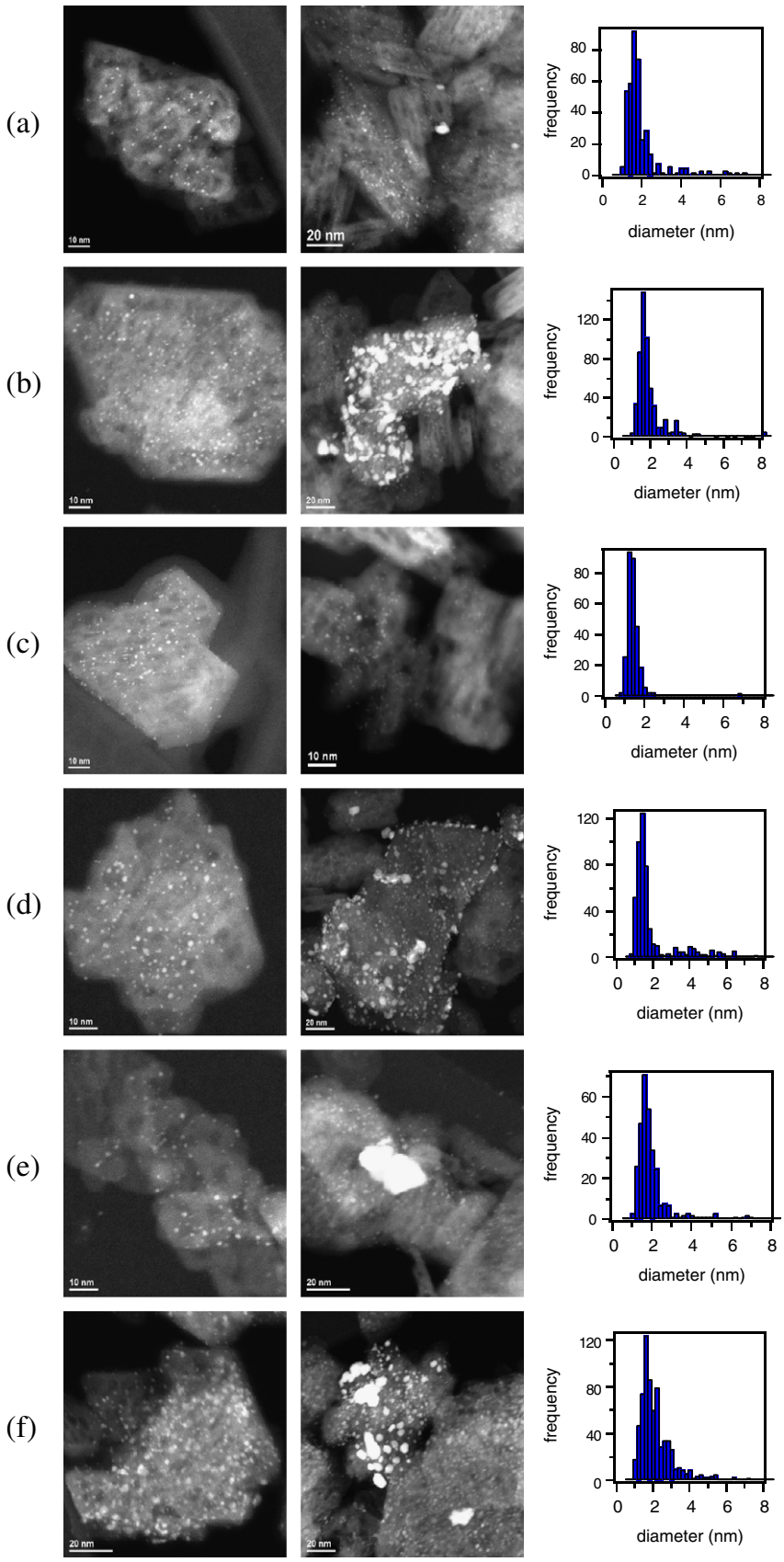

Fig. 2. TEM images and particle size distributions for the catalysts: (a) 1Pt/γ-Al_2O_3, (b) 1Pt–1Ni/γ-Al_2O_3, (c) 3Ni–1Pt/γ-Al_2O_3, (d) 1Pt–3Ni/γ-Al_2O_3, (e) 1Pt–3Ni(co-imp)/γ-Al_2O_3, (f) 1Pt–10Ni/γ-Al_2O_3.

bimetallic catalysts all show CO frequencies similar to that on Pt. This suggests that impregnation sequence does not significantly affect CO binding sites. One interpretation of this result could be that during reduction the atoms can migrate and that Ni atoms diffuse into the region beneath the surface while Pt atoms segregate to the surface. This is consistent with DFT predictions that, for Ni/Pt(1 1 1) surfaces, the segregation of Pt atoms to the top-most layer is thermodynamically favored both in the presence of atomic hydrogen and in vacuum [24]. The results found here for CO adsorption on the supported Pt/Ni catalysts are also in agreement with several other findings in literature. In our previous work studying the disproportionation of cyclohexene on monolayer bimetallic surfaces, it was found that disproportionation only took place on the Pt–Ni–Pt(1 1 1) surface [72]. In a follow-up work on supported Pt/Ni catalysts, the disproportionation of cyclohexene was observed, suggesting that the nanoparticles were Pt terminated [27]. The XPS studies by Mu et al. also showed that supported Pt/Ni catalysts were Pt-terminated after reduction [26].

3.2. Transmission electron microscopy (TEM)

High angle annular dark field (HAADF) TEM images and particle size distributions are shown in Fig. 2. The statistics from the particle size distribution are shown in Table 3. Particle size distributions were calculated by measuring horizontal particle diameters in several different images for each catalyst. Median particle sizes were found to be between 1.2 and 1.8 nm for the monometallic Pt catalyst and the five bimetallic catalysts. As seen in several of the images in Fig. 2, several larger particles are also present in all of the catalysts, which are the reason for the wide standard deviations in particle size shown in Table 3. EDS analysis (spectra not shown) on several large particles revealed that they were primarily composed of Pt, signifying that a fraction of the Pt in the catalysts has not been fully utilized since it is not completely alloyed with Ni and its presence in large particles reduces the number of active sites.

Table 3
Particle size distribution statistics.

Catalyst	Median diameter (nm)	Average diameter (nm)	Standard deviation in diameter (nm)
1Pt/γ-Al_2O_3	1.4	1.9	1.4
1Pt–1Ni/γ-Al_2O_3	1.6	1.9	1.4
1Pt–3Ni/γ-Al_2O_3	1.3	1.8	1.5
1Pt–10Ni/γ-Al_2O_3	1.8	2.1	1.3
3Ni–1Pt/γ-Al_2O_3	1.2	1.4	1.1
1Pt–3Ni(co-imp)/γ-Al_2O_3	1.6	1.9	1.3

3.3. Extended X-ray absorption fine structure (EXAFS)

Fig. 3a and b shows the Pt L_{III}-edge X-ray absorption near-edge structure (XANES) spectra of the two series of catalysts before and after reduction. Also, included in these figures are the spectra for Pt/γ-Al_2O_3 before and after reduction, and the Pt foil for reference. The background-subtracted, edge step normalized and k^2-weighted Pt L_{III}-edge EXAFS data ($\chi(k)$) are shown in R-space in Fig. 4a and b. The data were Fourier transformed using a k-range between 2 $Å^{-1}$ and 16 $Å^{-1}$ and the Hanning window function with sill width Δk = 2 $Å^{-1}$.

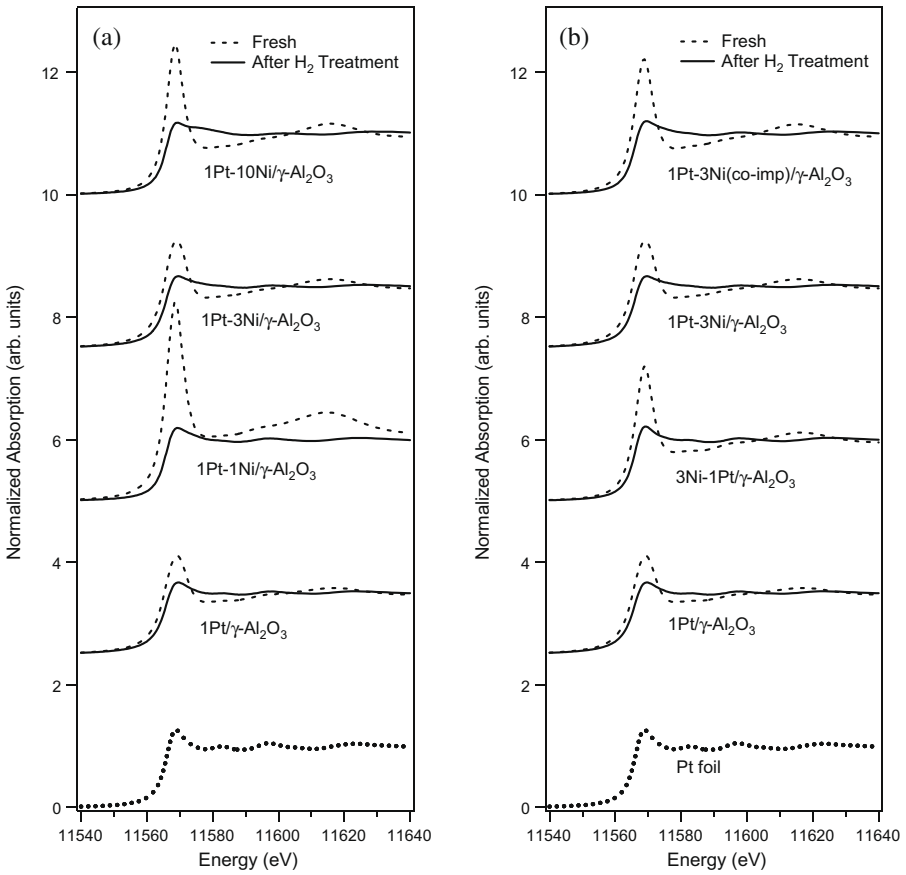

Fig. 3. Before and after reduction, Pt L_{III}-edge XANES spectra for (a) the series of bimetallic catalysts with different metal atomic ratios, (b) the series of bimetallic catalysts with different impregnation sequences. The Pt foil is included to serve as a reference for metallic Pt.

Examining the Pt L_{III}-edge XANES and EXAFS reveals information regarding the oxidation state of the samples [73]. Large Pt–O peaks are present at low radial distribution for all catalysts before reduction (Fig. 4a and b). After reduction in hydrogen, the Pt–O peaks disappear and Pt–M (M = Pt or Ni) peaks appear at slightly larger values of R. Similar conclusions can be drawn from the XANES data in Fig. 3a and b, where the white line intensity decreases toward that of Pt foil after reduction in H_2, indicating that the Pt has been reduced.

Fig. 5a and b presents the Fourier transformed experimental data after reduction for the two series of catalysts and the fits obtained using FEFF6 theory [66]. The results from the fitting procedure are summarized in Table 4. The EXAFS data were analyzed by including only Pt–Pt and Pt–Ni contributions. Based on the evidence from the XANES and EXAFS of the reduced samples discussed above, Pt–O contributions were neglected in the fitting of the reduced catalysts. For the bimetallic catalysts, the Pt–Pt distances presented in Table 4 range from 2.69 Å to 2.74 Å, which are 0.03 Å to 0.09 Å smaller than the metallic Pt–Pt distance (2.77 Å). Likewise, the Pt–Ni distances in Table 4 range from 2.55 Å to 2.58 Å, which are 0.06 Å to 0.09 Å larger than the metallic Ni–Ni distance (2.49 Å). These results confirm that Pt–Ni bimetallic bonds are present in the catalysts. Also, good fits to the Pt L_{III}-edge data could only be obtained by including both Pt–Pt and Pt–Ni contributions in the model, which strongly suggests that bimetallic bonds are present in the bimetallic nanoparticles.

The effect of impregnation sequence and metal atomic ratio can also be seen in Table 4. A trend is observed as the amount of Ni in the catalysts is increased. The 1Pt–1Ni/γ-Al_2O_3 catalyst has the smallest Pt–Ni coordination (1.2(5)) number, while the 1Pt–3Ni/γ-Al_2O_3 and 1Pt–10Ni/γ-Al_2O_3 catalysts have increasingly larger coordination numbers (2.6(6) and 5.5(8), respectively). This trend suggests that increasing the amount of Ni in the catalysts increases the extent of bimetallic formation. A trend also appears in the study of impregnation sequence. The 3Ni–1Pt/γ-Al_2O_3 (Pt-first) impregnation yields the lowest Pt–Ni coordination number (1.2(5)) while the 1Pt–3Ni/γ-Al_2O_3 (Ni-first) impregnation gives a larger Pt–Ni coordination number (2.6(6)); however, the 1Pt–3Ni(co-imp)/γ-Al_2O_3 catalyst shows the largest Pt–Ni coordination number (3.2(5)). This suggests that the co-impregnation leads to the highest extent of bimetallic formation among the three synthesis procedures.

The coordination numbers obtained from EXAFS analysis can be used to predict particle size using a correlation proposed by Frenkel et al. [74]. Assuming a hemispheric cuboctohedral geometry, this correlation predicts average particle sizes between 2.0 and 2.5 nm for the catalysts studied in these experiments. These values are slightly larger than the median and mean values obtained through TEM imaging (Table 3).

In all five of the bimetallic catalysts, the ratio of Pt–Pt to Pt–Ni coordination numbers is larger than the atomic ratios of Pt:Ni. For instance, the 1Pt–10Ni/γ-Al_2O_3 catalyst has Pt–Pt and Pt–Ni coordination numbers of 2.9 and 5.5, respectively, which yields a ratio of 1:1.9. This implies that the remaining Ni atoms are either located in monometallic Ni nanoparticles, dispersed across the γ-Al_2O_3 support, or present in the form of $NiAl_2O_4$.

3.4. Activity of benzene hydrogenation

Figs. 6a and 7a show the rates of benzene hydrogenation for the two series of bimetallic catalysts and the corresponding monometallic catalysts in the FTIR batch reactor. Cyclohexane was the only

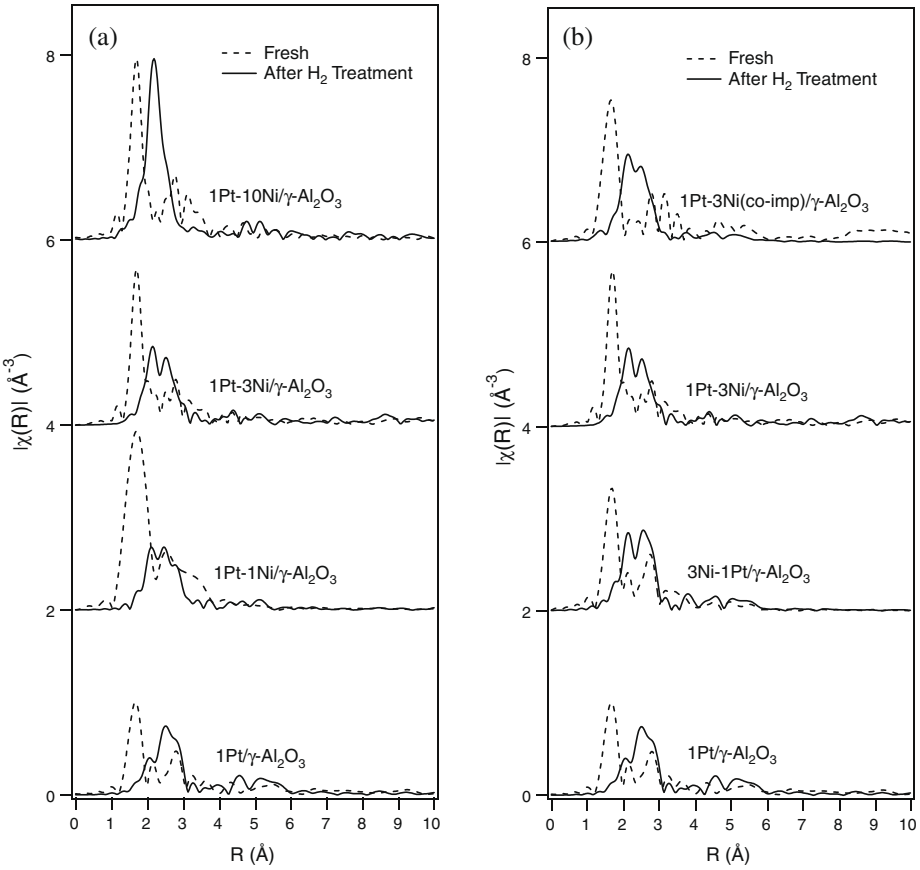

Fig. 4. Before and after reduction, Fourier transformed (magnitude) k^2-weighted EXAFS function ($\chi(k)$) of Pt L_{III}-edge of (a) the series of bimetallic catalysts with different metal atomic ratios and (b) the series of bimetallic catalysts with different impregnation sequences.

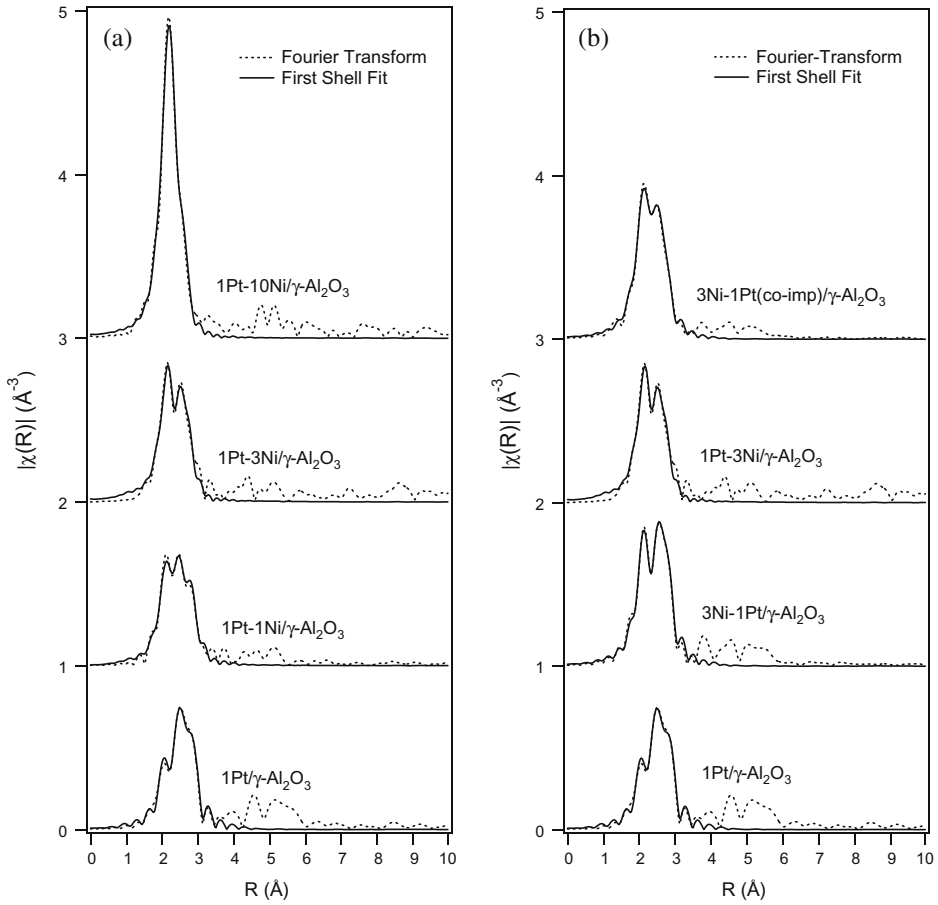

Fig. 5. Fourier transformed (magnitude) k^2-weighted EXAFS function ($\chi(k)$) of Pt L_{III}-edge of the catalysts after reduction for (a) the series of bimetallic catalysts with different metal atomic ratios, (b) the series of bimetallic catalysts with different impregnation sequences. Transformed data and fits are shown as dashed and solid lines, respectively.

Table 4
Summary of Pt L_{III}-edge fitting for 1Pt/γ-Al_2O_3 and Ni:Pt bimetallic catalysts.

Catalyst	1Pt/γ-Al_2O_3	1Pt–1Ni/γ-Al_2O_3	1Pt–3Ni/γ-Al_2O_3	1Pt–10Ni/γ-Al_2O_3	3Ni–1Pt/γ-Al_2O_3	1Pt–3Ni(co-imp)/γ-Al_2O_3
N(Pt–Pt)	6.2 ± 0.4	6.8 ± 0.7	4.4 ± 0.7	2.9 ± 1.4	7.3 ± 0.9	5.7 ± 0.9
N(Pt–Ni)	–	1.2 ± 0.5	2.6 ± 0.6	5.5 ± 0.8	1.4 ± 0.5	3.2 ± 0.5
R(Pt–Pt), Å	2.75 ± 0.01	2.73 ± 0.01	2.72 ± 0.01	2.69 ± 0.01	2.74 ± 0.01	2.72 ± 0.01
R(Pt–Ni), Å	–	2.58 ± 0.01	2.57 ± 0.01	2.55 ± 0.01	2.58 ± 0.01	2.58 ± 0.01
σ^2(Pt–Pt), Å^2	0.006 ± 0.001	0.008 ± 0.001	0.007 ± 0.001	0.007 ± 0.002	0.007 ± 0.001	0.007 ± 0.001
σ^2(Pt–Ni), Å^2	–	0.011 ± 0.003	0.010 ± 0.002	0.007 ± 0.001	0.008 ± 0.002	0.010 ± 0.001

observed reaction product, and the rates of cyclohexane production are presented in Figs. 6b and 7b. For both series of catalysts, it was observed that the rate of cyclohexane production over the bimetallic catalysts was greater than that of either monometallic Pt or Ni. The effect of impregnation sequence on activity is seen in Fig. 6a and b. The 3Ni–1Pt/γ-Al_2O_3 catalyst displays the lowest activity of the three bimetallic catalysts, while the 1Pt–3Ni/γ-Al_2O_3 shows intermediate activity, and the 1Pt–3Ni(co-imp)/γ-Al_2O_3 catalyst shows the highest activity.

From the series of catalysts with different Pt:Ni atomic ratios (Fig. 7a and b), the 1Pt–1Ni/γ-Al_2O_3 and 1Pt–3Ni/γ-Al_2O_3 catalysts are seen to have approximately the same hydrogenation activity, while the 1Pt–10Ni/γ-Al_2O_3 catalyst displays the highest activity. The activity of the 10Ni/γ-Al_2O_3 catalyst is also shown in these figures and it is interesting to note that it is completely inactive to benzene hydrogenation at this temperature.

In order to make quantitative comparisons, the rates of benzene hydrogenation were approximated by fitting the experimental data with first-order kinetics of the conversion of benzene. The first-order fit was performed over the entire curve of benzene consumption. Due to the excellent carbon balance over the duration of the hydrogenation reaction, the rate of benzene consumption should also be a good representation of the rate of cyclohexane production on each catalyst. The rate constants for the disappearance of benzene are listed in Table 5. In the series of catalysts used to study the effect of Pt:Ni ratio, the rate constants for benzene hydrogenation followed the order of 10Ni/γ-Al_2O_3 < 1Pt/γ-Al_2O_3 < 1Pt–1Ni/γ-Al_2O_3 ≈ 1Pt–3Ni/γ-Al_2O_3 < 1Pt–10Ni/γ-Al_2O_3. A similar trend in the Pt–Ni coordination number obtained from EXAFS was also observed for this series of bimetallic catalysts, showing that increasing the amount of Ni in the bimetallic catalysts increases the extent of Pt–Ni bimetallic bond formation, which in turn increases activity for benzene hydrogenation. Benzene hydrogenation rate constants were also observed to depend on impregnation sequence, where activity followed the order of 3Ni/γ-Al_2O_3 < 1Pt/γ-Al_2O_3 < 3Ni–1Pt/γ-Al_2O_3 < 1Pt–3Ni/γ-Al_2O_3 < 1Pt–3Ni(co-imp)/γ-Al_2O_3. The benzene hydrogenation activities for this series of catalysts also correlate with the Pt–Ni coordination numbers obtained through

EXAFS analysis, showing that the 1Pt–3Ni(co-imp)/γ-Al_2O_3 catalyst has both the highest activity and the largest Pt–Ni coordination number. This suggests that co-impregnation allows for the best mixing of metal atoms before they become fixed to the support during calcination.

3.5. Activity of 1,3-butadiene hydrogenation

The benzene hydrogenation studies showed that the bimetallic catalysts only slightly outperformed the monometallic catalysts. 1,3-Butadiene hydrogenation was chosen as a second probe reaction to further support the trends observed in benzene hydrogenation. Figs. 8a and 9a show the rates of 1,3-butadiene hydrogenation over the two series of catalysts studied. This work does not include an analysis of the selectivity of the catalysts, but the production and consumption of 1-butene and the production of *n*-butane are shown in Figs. 8b and 9b and 8c and 9c, respectively. Summing the total number of moles of carbon in 1,3-butadiene, 1-butene, and *n*-butane yielded a carbon balance that was accurate within the error of the experiments, supporting the assertion that 1-butene was the only butene present.

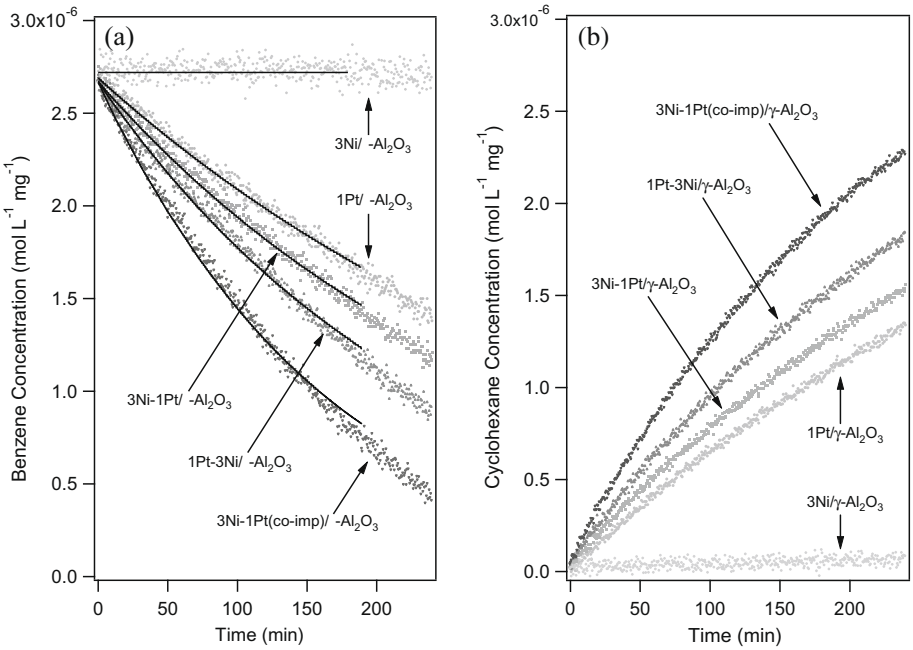

Fig. 6. The consumption of benzene (a) and production of cyclohexane (b) during the hydrogenation of benzene at 343 K for the series of catalysts with different impregnation sequences.

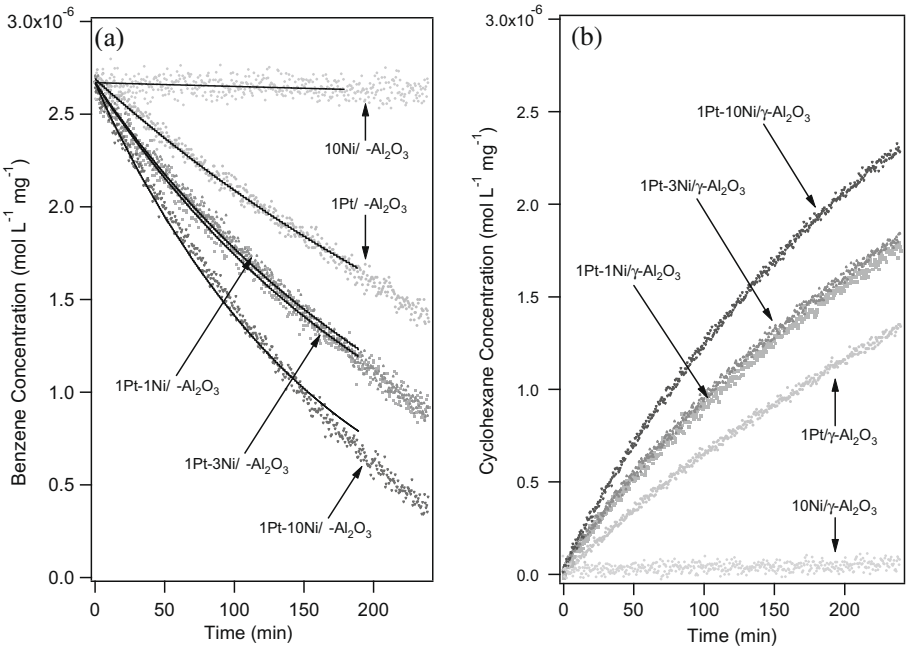

Fig. 7. The consumption of benzene (a) and production of cyclohexane (b) during the hydrogenation of benzene at 343 K for the series of catalysts with different metal atomic ratios.

Table 5
First-order consumption rate constants for the hydrogenation of benzene and 1,3-butadiene over the monometallic and bimetallic catalysts.

Catalyst	Benzene k (min^{-1})	1,3-Butadiene k (min^{-1})
$1Pt/\gamma\text{-}Al_2O_3$	2.5×10^{-3}	1.4×10^{-2}
$3Ni/\gamma\text{-}Al_2O_3$	~0	1.3×10^{-3}
$10Ni/\gamma\text{-}Al_2O_3$	~0	2.6×10^{-3}
$1Pt\text{–}1Ni/\gamma\text{-}Al_2O_3$	4.4×10^{-3}	4.0×10^{-2}
$1Pt\text{–}3Ni/\gamma\text{-}Al_2O_3$	4.1×10^{-3}	4.8×10^{-2}
$1Pt\text{–}10Ni/\gamma\text{-}Al_2O_3$	6.5×10^{-3}	1.6×10^{-1}
$3Ni\text{–}1Pt/\gamma\text{-}Al_2O_3$	3.4×10^{-3}	3.0×10^{-2}
$1Pt\text{–}3Ni(co\text{-}imp)/\gamma\text{-}Al_2O_3$	6.3×10^{-3}	9.9×10^{-2}

Figs. 8a and 9a show once again that both series of bimetallic catalysts outperform the monometallic Pt and Ni catalysts, and the trends in activity are similar to those observed for benzene hydrogenation. Approximating the experimental rates of 1,3-butadiene conversion with first-order kinetics yields the rate constants listed in Table 5. Similar to benzene hydrogenation, the following trend in rate constants is observed in the effect of Pt:Ni ratio: $10Ni/\gamma\text{-}Al_2O_3 < 1Pt/\gamma\text{-}Al_2O_3 < 1Pt\text{–}1Ni/\gamma\text{-}Al_2O_3 < 1Pt\text{–}3Ni/\gamma\text{-}Al_2O_3 < 1Pt\text{–}10Ni/\gamma\text{-}Al_2O_3$. In the study of impregnation sequence, the rate constants follow the trend of $3Ni/\gamma\text{-}Al_2O_3 < 1Pt/\gamma\text{-}Al_2O_3 < 3Ni\text{–}1Pt/\gamma\text{-}Al_2O_3 < 1Pt\text{–}3Ni/\gamma\text{-}Al_2O_3 < 1Pt\text{–}3Ni(co\text{-}imp)/\gamma\text{-}Al_2O_3$, which is also similar to the trend observed for benzene hydrogenation.

4. Discussion

Several parallels between model surfaces and supported catalysts can be drawn based on the results presented above. First, in the study of model Ni/Pt(1 1 1) surfaces, it was found that Pt atoms would segregate to the surface under reduction conditions [22]. Fig. 1a and b shows that this is also observed on supported catalysts. The spectra for bimetallic catalysts in Fig. 1a demonstrate that CO binds through surface Pt atoms, while the spectra in Fig. 1b show that regardless of impregnation sequence, catalysts of the same weight loading show similar CO vibrational frequencies, indicating that the catalyst surfaces have similar structures (namely Pt resides on the surface). Recent XPS studies on both polycrystalline Ni/Pt films [25] and on supported Pt/Ni nanoparticles [26] have also shown that Pt resides on the surface after reduction in H_2. Studies on model bimetallic systems have also demonstrated that Pt-terminated surfaces, either the Pt–Ni–Pt(1 1 1) prepared by deposition and subsequent diffusion of one monolayer (ML) Ni on Pt(1 1 1) or the Pt–Ni(1 1 1) surface pre-

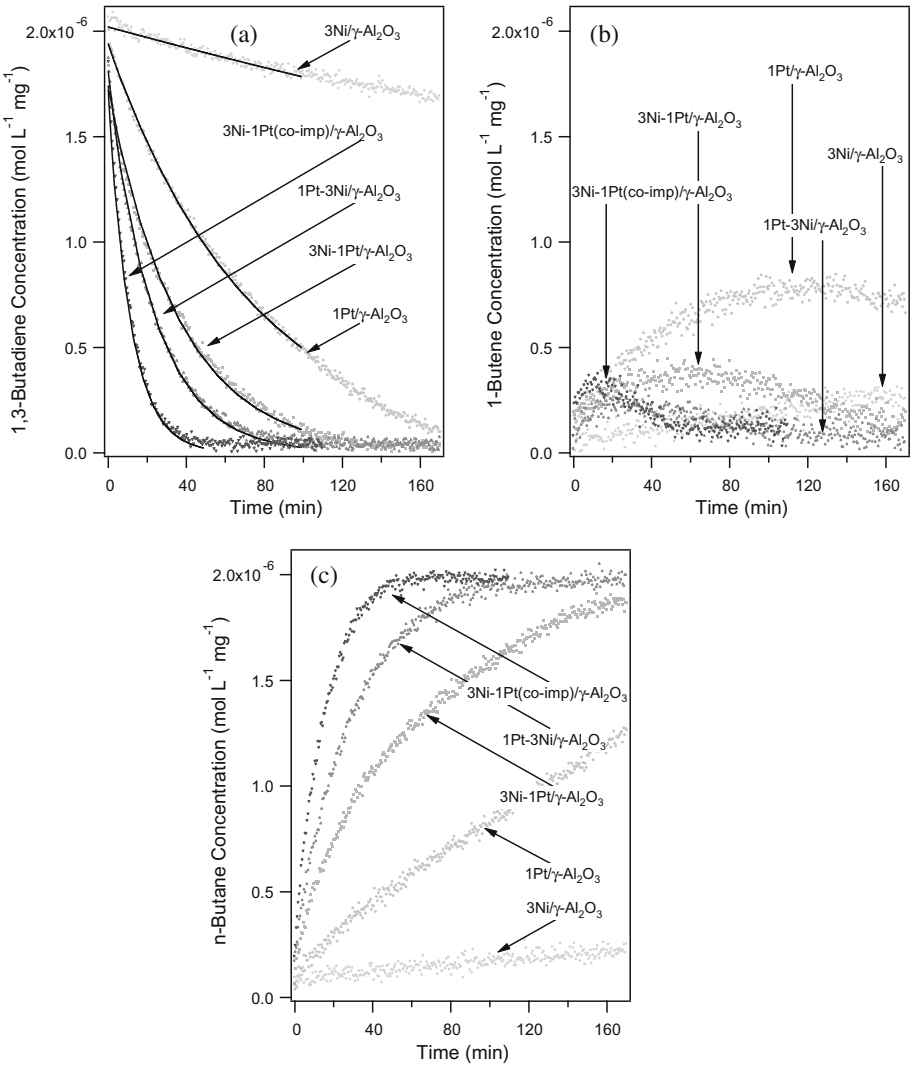

Fig. 8. The consumption of 1,3-butadiene (a), production and consumption of 1-butene (b), and production of *n*-butane (c) during the hydrogenation of 1,3-butadiene at 308 K for the series of catalysts with different impregnation sequences.

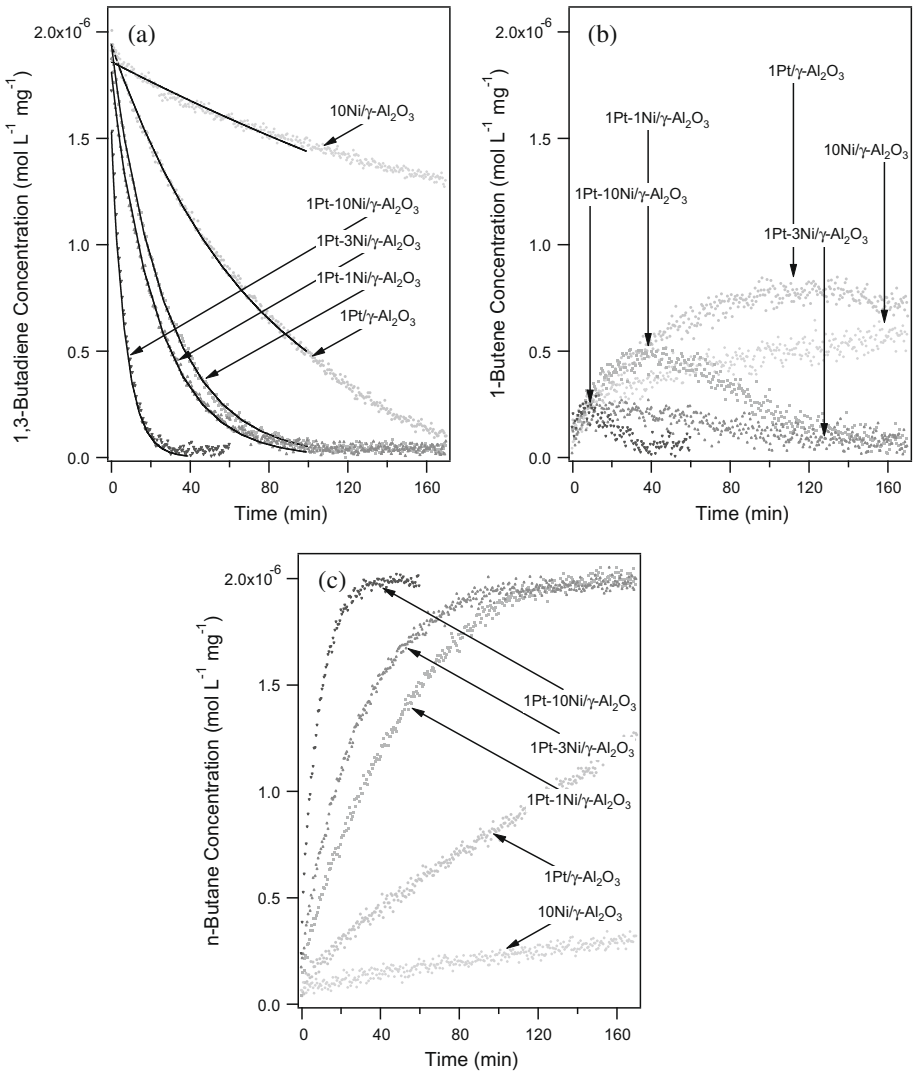

Fig. 9. The consumption of 1,3-butadiene (a), production and consumption of 1-butene (b), and production of *n*-butane (c) during the hydrogenation of 1,3-butadiene at 308 K for the series of catalysts with different metal atomic ratios.

pared by depositing ML Pt on Ni(1 1 1) [19], lead to novel low-temperature hydrogenation because they bind hydrogen and alkenes more weakly than either parent metal [75]. This effect was also observed in both the hydrogenation of benzene and 1,3-butadiene, where the bimetallic catalysts were seen to be more active than either of the corresponding monometallic catalysts.

Surface science and DFT studies have observed that the strain effect from the lattice mismatch can modify the electronic structure of metals, which contributes to the novel activity observed on monolayer bimetallic catalysts [60,76,77]. The Pt–Pt interatomic distances obtained through EXAFS fitting (Table 4) suggest that Pt atoms in the bimetallic catalysts are in a strained state (the bulk Pt–Pt distance is 2.77 Å; the Pt–Pt distance in the Pt/γ-Al_2O_3 catalyst is 2.75 Å). It is more interesting to note that as Pt:Ni ratio is increased from 1:1 to 1:10, the Pt–Pt interatomic distance decreases from 2.73 Å to 2.69 Å., demonstrating that Pt atoms are under greater strain as the extent of bimetallic bond formation increases. If the surfaces of the bimetallic nanoparticles were terminated by Ni atoms, such a large strain effect should not be noticeable in the Pt–Pt interatomic distances. A monolayer of larger atoms (Pt) on top of smaller ones (Ni) would cause a much greater strain, as seen in the Pt–Pt interatomic distances, supporting the assertion that Pt atoms reside on the surface of the bimetallic nanoparticles (as shown in FTIR spectroscopy of adsorbed CO). Additionally, the structure of the 1Pt–10Ni/γ-Al_2O_3 catalyst may mimic the Pt/Ni(1 1 1) surfaces studied by Khan and co-workers, in which strain effects were identified as one of the possible reasons for the enhanced hydrogenation activity [19]. The correlations between the model surfaces and supported catalysts provide a useful example of how better hydrogenation catalysts can potentially be designed based on information from DFT modeling and surface science studies.

The results presented in this paper clearly show that bimetallic catalysts exhibit higher hydrogenation activity than the corresponding monometallic catalysts for the hydrogenation of conjugated C=C bonds. In studying the effect of metal atomic ratio and impregnation sequence, this work also shows that the hydrogenation activity is increased by either increasing Ni loading or using a simultaneous co-impregnation. It is very interesting to note that the increasing activity in each series of catalysts also corresponds to an increasing number of Pt–Ni nearest neighbors from EXAFS, confirming conclusively that the hydrogenation activity is directly related to the extent of the Pt–Ni bimetallic bond formation.

5. Conclusions

Pt/Ni bimetallic catalysts were synthesized in order to study the effects of metal atomic ratio and impregnation sequence. The bimetallic catalysts were more active than either parent metal catalyst for both benzene and 1,3-butadiene hydrogenation. In studying the effect of metal atomic ratio, it was found that hydrogenation activity increased with increasing Ni loading. Similarly, it was found that the catalyst synthesized by co-impregnation exhibited the highest activity in comparison with either sequentially impregnated catalyst. Hydrogenation activity was also seen to correlate to Pt–Ni coordination numbers calculated from EXAFS measurements. FTIR CO adsorption results suggest that Pt resides on the surface of bimetallic nanoparticles and that the Pt atoms can segregate during reduction at high temperatures, which is consistent with previous DFT modeling and surface science studies in which the Pt-terminated surface is thermodynamically stable under reducing environment.

Acknowledgments

The authors acknowledge financial support from the US Department of Energy, Office of Sciences, Division of Chemical Sciences (Grant# FG02-03ER15468). Use of the National Synchrotron Light Source, Brookhaven National Laboratory, for the EXAFS experiments was supported by the US Department of Energy, Office of Basic Energy Sciences (Grant# DE-FG02-05ER15688).

References

[1] J.H. Sinfelt, Bimetallic Catalysts: Discoveries, Concepts, and Applications, Wiley, New York, 1983.
[2] J.A. Rodriguez, Surface Science Reports 24 (1996) 223.
[3] J.G. Chen, C.A. Menning, M.B. Zellner, Surface Science Reports 63 (2008) 201.
[4] G.W. Huber, J.W. Shabaker, S.T. Evans, J.A. Dumesic, Applied Catalysis B 62 (2006) 226.
[5] N.M. Markovic, P.N. Ross, Surface Science Reports 45 (2002) 121.
[6] E. Iglesia, S.L. Soled, R.A. Fiato, G.H. Via, Journal of Catalysis 143 (1993) 345.
[7] B. Hammer, J.K. Nørskov, Surface Science 343 (1995) 211.
[8] D.W. Goodman, Journal of Physical Chemistry 100 (1996) 13090.
[9] B. Hammer, J.K. Nørskov, Advances in Catalysis 45 (2000) 71.
[10] M. Neurock, V. Pallassana, R.A. van Santen, Journal of the American Chemical Society 122 (2000) 1150.
[11] Y. Xu, A.V. Ruban, M. Mavrikakis, Journal of the American Chemical Society 126 (2004) 4717.
[12] J. Greeley, M. Mavrikakis, Nature Materials 3 (2004) 810.
[13] H.H. Hwu, J. Eng, J.G. Chen, Journal of the American Chemical Society 124 (2002) 702.
[14] N.A. Khan, H.H. Hwu, J.G. Chen, Journal of Catalysis 205 (2002) 259.
[15] J.R. Kitchin, N.A. Khan, M.A. Barteau, J.G. Chen, B. Yakshinksiy, T.E. Madey, Surface Science 544 (2003) 295.
[16] O. Skoplyak, M.A. Barteau, J.G. Chen, Journal of Physical Chemistry B 110 (2006) 1686.
[17] M.P. Humbert, J.G. Chen, Journal of Catalysis 257 (2008) 297.
[18] L.E. Murillo, A.M. Goda, J.G. Chen, Journal of the American Chemical Society 129 (2007) 7101.
[19] N.A. Khan, M.B. Zellner, J.G. Chen, Surface Science 556 (2004) 87.
[20] O. Skoplyak, M.A. Barteau, J.G. Chen, ChemSusChem 1 (2008) 524.
[21] J.R. Kitchin, J.K. Nørskov, M.A. Barteau, J.G. Chen, Journal of Chemical Physics 120 (2004) 10240.
[22] C.A. Menning, J.G. Chen, Journal of Chemical Physics 130 (2009) 174709.
[23] C.A. Menning, H.H. Hwu, J.G. Chen, Journal of Physical Chemistry B 110 (2006) 15471.
[24] C.A. Menning, J.G. Chen, Journal of Chemical Physics 128 (2008) 164703.
[25] C.A. Menning, J.G. Chen, Journal of Power Sources 195 (2010) 3140.
[26] R.T. Mu, Q. Fu, H.Y. Liu, D.L. Tan, R.S. Zhai, X.H. Bao, Applied Surface Science 255 (2009) 7296.
[27] Y.Y. Shu, L.E. Murillo, J.P. Bosco, W. Huang, A.I. Frenkel, J.G. Chen, Applied Catalysis A 339 (2008) 169.
[28] A. Stanislaus, B.H. Cooper, Catalysis Reviews – Science and Engineering 36 (1994) 75.
[29] B.H. Cooper, B.B.L. Donnis, Applied Catalysis A 137 (1996) 203.
[30] G. Bellussi, C. Perego, Cattech 4 (2000) 4.
[31] H.A. Franco, M.J. Phillips, Journal of Catalysis 63 (1980) 346.
[32] R.Z.C. Vanmeerten, J.W.E. Coenen, Journal of Catalysis 37 (1975) 37.
[33] R.Z.C. Vanmeerten, A.C.M. Verhaak, J.W.E. Coenen, Journal of Catalysis 44 (1976) 217.
[34] A. Jasik, R. Wojcieszak, S. Monteverdi, M. Ziolek, M.M. Bettahar, Journal of Molecular Catalysis A 242 (2005) 81.
[35] A. Louloudi, N. Papayannakos, Applied Catalysis A 204 (2000) 167.
[36] A. Louloudi, J. Michalopoulos, N.H. Gangas, N. Papayannakos, Applied Catalysis A 242 (2003) 41.
[37] G. Marcelin, R.F. Vogel, H.E. Swift, Journal of Catalysis 98 (1986) 64.
[38] R. Molina, G. Poncelet, Journal of Catalysis 199 (2001) 162.
[39] S. Toppinen, T.K. Rantakyla, T. Salmi, J. Aittamaa, Industrial & Engineering Chemistry Research 35 (1996) 1824.
[40] J.M. Basset, G. Dalmaiimelik, M. Primet, R. Mutin, Journal of Catalysis 37 (1975) 22.
[41] S.D. Lin, M.A. Vannice, Journal of Catalysis 143 (1993) 539.
[42] P. Chou, M.A. Vannice, Journal of Catalysis 107 (1987) 129.
[43] P. Chou, M.A. Vannice, Journal of Catalysis 107 (1987) 140.
[44] C. Milone, G. Neri, A. Donato, M.G. Musolino, Journal of Catalysis 159 (1996) 253.
[45] L. Ronchin, L. Toniolo, Catalysis Today 66 (2001) 363.
[46] J.Q. Wang, P.J. Guo, S.R. Yan, M.H. Qiao, H.X. Li, K.N. Fan, Journal of Molecular Catalysis A 222 (2004) 229.
[47] P. Kluson, L. Cerveny, Applied Catalysis A 128 (1995) 13.
[48] R. Badillaohlbaum, H.J. Neuburg, W.F. Graydon, M.J. Phillips, Journal of Catalysis 47 (1977) 273.
[49] M.J. Phillips, P.H. Emmett, Journal of Catalysis 101 (1986) 268.
[50] K.J. Yoon, M.A. Vannice, Journal of Catalysis 82 (1983) 457.
[51] S.W. Ho, J.M. Cruz, M. Houalla, D.M. Hercules, Journal of Catalysis 135 (1992) 173.
[52] J.M. Jablonski, D. Potocznapetru, J. Okal, L. Krajczyk, Reaction Kinetics and Catalysis Letters 54 (1995) 15.
[53] W.F. Taylor, Journal of Catalysis 9 (1967) 99.
[54] W.F. Taylor, H.K. Staffin, Journal of Physical Chemistry 71 (1967) 3314.
[55] L.J. Simon, P.J. Kooyman, J.G. van Ommen, J.A. Lercher, Applied Catalysis A 252 (2003) 283.
[56] D. Seth, A. Sarkar, F.T.T. Ng, G.L. Rempel, Chemical Engineering Science 62 (2007) 4544.
[57] J. Goetz, D.Y. Murzin, M. Ulischenko, R. Touroude, Chemical Engineering Science 51 (1996) 2879.
[58] M. Benkhaled, C. Descorme, D. Duprez, S. Morin, C. Thomazeau, D. Uzio, Applied Catalysis A 346 (2008) 36.
[59] J. Silvestre-Albero, G. Rupprechter, H.J. Freund, Journal of Catalysis 240 (2006) 58.
[60] J.C. Bertolini, Applied Catalysis A 191 (2000) 15.
[61] A. Sarkany, G. Stefler, J.W. Hightower, Applied Catalysis A 127 (1995) 77.
[62] P. Basu, T.H. Ballinger, J.T. Yates, Review of Scientific Instruments 59 (1988) 1321.
[63] S.E. Stein, Infrared Spectra, in: P.J. Linstrom, W.G. Mallard (Eds.), NIST Chemistry WebBook, NIST Standard Reference Database Number 69, National Institute of Standards and Technology, Gaithersburg, MD, 20899. Available from: <http://webbook.nist.gov>. Retrieved 8 November 2008.
[64] M. Newville, Journal of Synchrotron Radiation 8 (2001) 322.
[65] B. Ravel, M. Newville, Journal of Synchrotron Radiation 12 (2005) 537.
[66] J.J. Rehr, R.C. Albers, Reviews of Modern Physics 72 (2000) 621.
[67] M. Primet, J.M. Basset, M.V. Mathieu, M. Prettre, Journal of Catalysis 29 (1973) 213.
[68] S.D. Jackson, B.M. Glanville, J. Willis, G.D. Mclellan, G. Webb, R.B. Moyes, S. Simpson, P.B. Wells, R. Whyman, Journal of Catalysis 139 (1993) 207.
[69] B.A. Riguetto, S. Damyanova, G. Gouliev, C.M.P. Marques, L. Petrov, J.M.C. Bueno, Journal of Physical Chemistry B 108 (2004) 5349.
[70] G. Poncelet, M.A. Centeno, R. Molina, Applied Catalysis A 288 (2005) 232.
[71] Y.G. Chen, J. Ren, Catalysis Letters 29 (1994) 39.
[72] N.A. Khan, M.B. Zellner, L.E. Murillo, J.G. Chen, Catalysis Letters 95 (2004) 1.
[73] A. Jentys, B.J. Mchugh, G.L. Haller, J.A. Lercher, Journal of Physical Chemistry 96 (1992) 1324.
[74] A.I. Frenkel, C.W. Hills, R.G. Nuzzo, Journal of Physical Chemistry B 105 (2001) 12689.
[75] M.P. Humbert, L.E. Murillo, J.G. Chen, ChemPhysChem 9 (2008) 1262.
[76] M. Mavrikakis, B. Hammer, J.K. Nørskov, Physical Review Letters 81 (1998) 2819.
[77] J.R. Kitchin, J.K. Nørskov, M.A. Barteau, J.G. Chen, Physical Review Letters 93 (2004) 156801.